

## Nanotubes from the misfit compound alloy LaS-NbTaS

Dalit Stolovas, Marco Serra, Ronit Popovitz-Biro, Iddo Pinkas, Lothar Houben, José J. Calvino, Ernesto Joselevich, Reshef Tenne, Raul Arenal, and Luc Lajaunie

*Chem. Mater.*, **Just Accepted Manuscript** • DOI: 10.1021/acs.chemmater.8b03632 • Publication Date (Web): 21 Nov 2018

Downloaded from <http://pubs.acs.org> on November 25, 2018

### Just Accepted

“Just Accepted” manuscripts have been peer-reviewed and accepted for publication. They are posted online prior to technical editing, formatting for publication and author proofing. The American Chemical Society provides “Just Accepted” as a service to the research community to expedite the dissemination of scientific material as soon as possible after acceptance. “Just Accepted” manuscripts appear in full in PDF format accompanied by an HTML abstract. “Just Accepted” manuscripts have been fully peer reviewed, but should not be considered the official version of record. They are citable by the Digital Object Identifier (DOI®). “Just Accepted” is an optional service offered to authors. Therefore, the “Just Accepted” Web site may not include all articles that will be published in the journal. After a manuscript is technically edited and formatted, it will be removed from the “Just Accepted” Web site and published as an ASAP article. Note that technical editing may introduce minor changes to the manuscript text and/or graphics which could affect content, and all legal disclaimers and ethical guidelines that apply to the journal pertain. ACS cannot be held responsible for errors or consequences arising from the use of information contained in these “Just Accepted” manuscripts.

# Nanotubes from the misfit compound alloy $\text{LaS-Nb}_x\text{Ta}_{(1-x)}\text{S}_2$

Dalit Stolovas<sup>†,‡</sup>, Marco Serra<sup>†,‡</sup>, Ronit Popovitz-Biro<sup>†</sup>, Iddo Pinkas<sup>‡</sup>, Lothar Houben<sup>‡</sup>, José J. Calvino<sup>§,||</sup>, Ernesto Joselevich<sup>†</sup>, Reshef Tenne<sup>†,\*</sup>, Raul Arenal<sup>†,¶</sup> and Luc Lajaunie<sup>§,||,##</sup>

<sup>†</sup> Department of Materials and Interfaces, Weizmann Institute, Rehovot 76100, Israel

<sup>‡</sup> Department of Chemical Research Support, Weizmann Institute, Rehovot 76100, Israel

<sup>§</sup> Departamento de Ciencia de los Materiales e Ingeniería Metalúrgica y Química Inorgánica, Facultad de Ciencias, Universidad de Cádiz, Campus Río San Pedro S/N, Puerto Real 11510, Cádiz, Spain

<sup>||</sup> Instituto Universitario de Investigación de Microscopía Electrónica y Materiales (IMEYMAT), Facultad de Ciencias, Universidad de Cádiz, Campus Río San Pedro S/N, Puerto Real 11510, Cádiz, Spain

<sup>\*</sup> Laboratorio de Microscopías Avanzadas, Instituto de Nanociencia de Aragón, Universidad de Zaragoza, 50018 Zaragoza, Spain

<sup>¶</sup> ARAID Foundation, 50018 Zaragoza, Spain

**ABSTRACT:** Misfit layered compounds (MLC) with the composition  $(\text{LaS})_{1.15}\text{TaS}_2$  (for simplicity denoted as  $\text{LaS-TaS}_2$ ) and  $\text{LaS-NbS}_2$  were prepared and studied in the past. Nanotubes of  $\text{LaS-TaS}_2$  could be easily synthesized, while tubular structure of the  $\text{LaS-NbS}_2$  were found to be rather rare in the product. In order to understand this riddle, quaternary alloys of  $\text{LaS-Nb}_x\text{Ta}_{(1-x)}\text{S}_2$  with ascending Nb concentration were prepared herein in the form of nanotubes (and platelets). Not surprisingly, the concentration of these quaternary nanotubes shrank (and the relative density of platelets increased) with increasing Nb content in the precursor. The structure and chemical composition of such nanotubes was elucidated by electron microscopy. Conceivably, the  $\text{TaS}_2$  in the MLC compounds  $\text{LnS-TaS}_2$  (Ln=lanthanide atom) crystallizes in the  $2H$  polytype. High resolution transmission electron microscopy showed however that, invariably MLC nanotubes prepared from 80 at% Nb content in the precursor belonged to the  $1T$  polytype. Raman spectroscopy of individual tubes revealed that up to 60 at% Nb, they obey the standard model of MLC, while higher Nb lead to large deviations which are discussed in brief. The analysis indicated also that such nanotubes do not exhibit the pattern assigned to charge density wave transition so typical for binary  $1T\text{-TaS}_2$ . The prospect for revealing interesting quasi-1D behavior of such quaternary nanotubes is also briefly discussed.

## INTRODUCTION

Chrysotile ( $\text{Mg}_3(\text{Si}_2\text{O}_5)(\text{OH})_4$ ) and kaolinite (hallyosite- $\text{Al}_2\text{Si}_2\text{O}_5(\text{OH})_4$ ) are well-studied layered clay minerals which are found in nature sometime in the form of nanotubes or nanoscrolls. Each chrysotile  $TO$  layer consists of a sheet of magnesia octahedra ( $O$ ), which is linked to a sheet of silica tetrahedra ( $T$ ) by sharing one (apical) oxygen atom. The equilibrium lattice parameters of the  $T$  and  $O$  sheets are 5.317 and 5.432 Å, respectively.<sup>1</sup> This asymmetry leads to a strain in the (so-called lizardite)  $TO$  slab. Pauling argued that layered compounds with asymmetric structure along the  $c$ -axis, like chrysotile would tend to relax the strain through folding.<sup>2</sup> This hypothesis was confirmed twenty years afterwards by direct observation of the chrysotile nanotubes.<sup>3,4</sup> A complementary impetus for the formation of hollow closed structures from 2D materials was proposed by Kroto,<sup>5</sup> who argued that graphene layers would not be stable towards folding, due to the preeminence of the chemical energy stored in the dangling bonds of the rim atoms. This hypothesis, initially aimed at explaining the stability of  $\text{C}_{60}$ . It was later-on expanded to include carbon nanotubes,<sup>6</sup> inorganic fullerene-like structures (IF) and nanotubes (INT) from  $\text{WS}_2$ ,<sup>7</sup> and subsequently from

numerous other 2D materials.<sup>8</sup> Ultimately, the goal would be to unify these two different driving forces and synthesize nanotubes from 2D materials that are asymmetric along the  $c$ -axis in a controlled way and consequently in high yields. In this respect, misfit layered compounds (MLC)<sup>9,10</sup> come into play. Misfit nanotubes hold promise for applications in the fields of optoelectronics and thermoelectrics.<sup>11,12</sup>

Chalcogenide-based MLC are materials made of alternating monolayers of a compound with distorted rocksalt structure MX, like LaS, and a  $\text{TX}_2$  slab with hexagonal structure, like  $\text{TaS}_2$ . MLC have the general formula  $[(\text{MX})_{1+y}]_m[\text{TX}_2]_n$  with  $0.08 < y < 0.28$ , denoted for simplicity  $\text{MX-TX}_2$ .<sup>9,10,13–20</sup> **Figure 1a** shows a schematic drawing of an MLC lattice. Generally, the interlayer spacing ( $c$ -axis) in the MLC is common to the two sublayers. The  $b$ -axis of the ortho-pseudo-hexagonal unit cell of the  $\text{TaS}_2$  ( $\sqrt{3}a$ ) lattice (**Figure 1b**) coincides with the  $b$ -axis of LaS (**Figure 1c**). The  $a$ -axis is incommensurate and the  $a_{\text{MX}}/a_{\text{TX}_2}$  ratio is an irrational number close to  $5/3$ . Therefore, the lattice of MLC does not have a translational symmetry along the  $a$ -axis and a well-defined unit cell. Rather, these compounds are represented as approximants, having for example three units of LaS along the  $a$ -axis and five units of  $\text{TaS}_2$ . Like many other

layered compounds, layers in MLC are held together via weak van der Waals forces. In addition, the different work-function of the two subunits leads to partial charge transfer between the subunits. Consequently, polar forces arise between the two subunits, which add extra stability to the 2D superstructure of MLC. Thus MLC can be considered as intercalation compounds in which the guest MX layer donates, commonly, electron charge to the hexagonal host  $\text{TX}_2$  lattice. It was recently demonstrated that, under proper conditions, many ternary MLC compounds can form nanotubes or nanoscrolls in high yields.<sup>11,21</sup> Here, the two main mechanisms for the formation of the MLC nanotubes are the asymmetry along the  $c$ -axis juxtaposed with the large chemical energy stored in the dangling bonds of the rim atoms.<sup>8</sup>

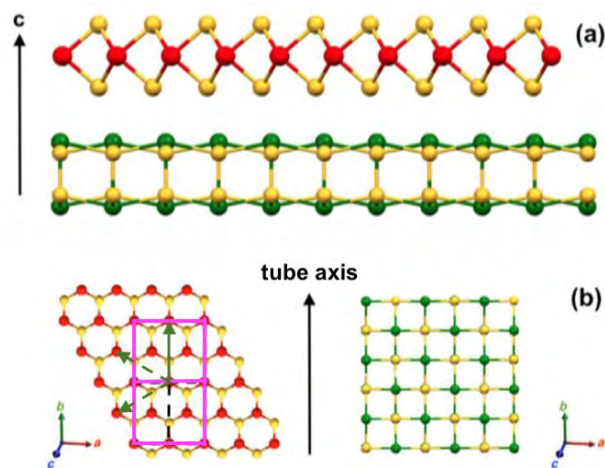


**Figure 1.** a. Schematic rendering of a lattice of the  $(\text{MX})_{1+y}(\text{TX}_2)$  misfit layered compound. Green, red and yellow circles are T, M and X atoms respectively; b.  $\text{LaS}_2$  and c.  $\text{LaS}$  lattices viewed from the  $\langle 001 \rangle$  direction. The hexagonal and the ortho-pseudohexagonal (purple) lattices of the  $\text{TaS}_2$  are shown.

In preparing nanotubes from ternary MLC, differences in the yield of the synthesized nanotubes were noticed between compounds of a similar composition. For instance, while  $\text{LaS-TaS}_2$  tubes were obtained in high yields (ca. 50%), the tubes from  $\text{HoS-TaS}_2$  were produced, under equivalent conditions, in small yields of about 5%<sup>22</sup> and merely a 1% yield for  $\text{CeS-TaS}_2$ <sup>8</sup> and  $\text{YbS-TaS}_2$ <sup>23</sup> nanotubes. Furthermore, nanotubes from  $\text{LaS-NbS}_2$  could be barely observed in the reaction product, although  $\text{PbS-NbS}_2$  nanotubes were produced in high yields.<sup>20</sup> These observations cannot be easily addressed, since the respective Ta- and Nb-based MLC are well established in the bulk form.<sup>9,24–26</sup> Obviously, these differences could be attributed to the limited number of experiments which spanned a small fraction of the possible phase-space of such reactions. Nevertheless, they could also reflect more fundamental structural or chemical reactivity differences, which warranted further investigation. For example, the Ta-S bond is known to have greater ionic character than the Nb-S bond in the layered  $\text{MS}_2$  compound.<sup>27</sup> Therefore, the intercalation of tin atoms was found to be easier in  $\text{NbS}_2$  than in  $\text{TaS}_2$ .<sup>28</sup> Towards that goal, a series of quaternary compounds of the composition  $\text{LaS-Nb}_x\text{Ta}_{1-x}\text{S}_2$   $0 < x < 1$  were prepared and studied in detail.

Nanotubes were found to become a scarcity with increasing Nb content of the reaction mixture. Electron microscopy and Raman analyses help shedding some light on the structure and reactivity of such nanotubes with increasing Nb and decreasing Ta content. Noticeably, very few works were dedicated to the alloyed 2D materials  $\text{Nb}_x\text{Ta}_{1-x}\text{S}_2$  and selenides thereof. For example, the charge density wave structure of  $1T$  alloys with  $x < 0.1$  were studied with scanning tunneling microscopy (STM).<sup>29</sup> In a more recent work, the non-linear optical properties of  $\text{Nb}_{0.5}\text{Ta}_{0.5}\text{S}_2$  nanotubes and Haeckelites were calculated.<sup>30</sup> To the best of our knowledge, quaternary MLC of the type  $\text{LaS-Nb}_x\text{Ta}_{1-x}\text{S}_2$  were not described in the literature in the bulk form or as nanotubes prior to this work.

## EXPERIMENTAL

### Synthesis of $\text{LaS-Nb}_x\text{Ta}_{(1-x)}\text{S}_2$ nanotubes

The nanotubes were prepared following a synthetic protocol similar to the method reported before for the preparation of  $\text{LnS-TaS}_2$  nanotubes,<sup>8</sup> however with an improved temperature control. The synthesis of  $\text{LaS-Nb}_x\text{Ta}_{(1-x)}\text{S}_2$  ( $0.0 \leq x \leq 0.9$ ) nanotubes was performed by means of chemical vapour transport reaction starting from a mixture of La (Strem Chemicals 99.9%), Ta (Alfa Aesar 99.9%), Nb (Sigma Aldrich 99.8%) and S (Sigma Aldrich 99.98%), in the presence of a small amount (2 mg, 5  $\mu\text{mol}$ ) of  $\text{TaCl}_5$  (Sigma Aldrich 99.99%) as catalyst. While the niobium content was increased gradually from 10 at% to 90 at% that of tantalum was reduced (from 90 at% to 10 at%), correspondingly. The powders were mixed in a mortar in the proportion 1:1:3 (25 mg, 0.13 mmol Ta: 19.2 mg, 0.13 mmol La: 13.2 mg, 0.41 mmol S) and placed in a quartz ampoule in a glove box under nitrogen atmosphere in order to prevent the oxidation of the reactants. For the Nb-containing samples, a certain percentage of Ta (10 at%, 20 at%, 40 at%, 60 at%, 80 at% and 90 at%) was replaced by the corresponding molar amount of Nb at% (= 100 - at% of Ta). The quartz ampoules were sealed under vacuum at a pressure on the order of  $1 \times 10^{-5}$  Torr using a vacuum setup consisting of a rotary pump and diffusion pump equipped with liquid  $\text{N}_2$  trap. The high-temperature annealing was carried-out in a vertical furnace in two steps using two opposite gradients of temperatures. First, the ampoules were submitted to a thermal gradient 350 °C at the bottom edge and 800 °C at the upper edge. After 1 h the ampoules were moved inside the bore of the furnace and exposed to an opposite temperature gradient between 857 °C at the bottom part and 400 °C at the upper part. After 6 h the ampoules were removed from the furnace and were allowed to cool down to room temperature overnight. The products were accumulated in the lower edge of the ampoule. Under these experimental conditions the mass transport to the upper edge of the ampoule was negligible as previously reported.<sup>23</sup>

### Characterization

#### Electron microscopy analysis

Scanning electron microscopy (SEM) was done by LEO model Supra 55VP SEM. Transmission electron microscopy (TEM) including selected area electron diffraction (SAED) analyses and energy dispersive x-ray spectroscopy analysis

(EDS/TEM), was performed using a JEOL JEM2100 (operating at 200 kV) equipped with Thermo Fisher retractable EDS detector. A FEI Tecnai F20 microscope (200 kV) was used for high-resolution TEM (HRTEM), scanning TEM (STEM) imaging and electron diffraction (ED). Nanobeam ED images were recorded in STEM microprobe mode on a Gatan Orius 600 A CCD camera.

It is important to note that, while the SEM study was carried-out on native samples, the TEM analyses were performed on samples which were dispersed in solution by sonication. Therefore, the samples analyzed by the two techniques cannot be considered identical. For example, while many nanotubes with diameter below 100 nm were observed by SEM almost in each sample, this was not the case for the TEM analysis, where only nanotubes with diameter exceeding 150 nm could be analyzed.

#### High-resolution transmission electron microscopy

High-resolution scanning TEM (HRSTEM) imaging and spatially-resolved electron energy-loss spectroscopy (SR-EELS) were performed using a FEI Titan Low-Base and a FEI Titan Themis microscope which were operated at 200 kV. The Low-Base is equipped with a  $C_s$  probe corrector, a monochromator, an ultra-bright X-FEG electron source, an energy dispersive x-ray spectrometry (EDS) detector and a Gatan Tridiem ESR 865 EELS spectrometer. The Themis is equipped with a double  $C_s$  aberration-corrector, a monochromator, a X-FEG gun, an Ultra High Resolution Energy Filter (Gatan Quantum ERS) which allows working in Dual-EELS mode and a Super X EDS detector, which consists of a 4-windowless detector that can be used independently. Quantitative spatially-resolved (SR) EDS analyses were performed on the Themis microscope by using the Super X detector and the VELOX software. EDS quantification of the samples was performed by using the S-K, Nb-K, Ta-L and La-L lines. Due to the proximity of the Ta-L and Cu-L lines, the Cu signal (which can arise from the TEM column and sample holder) was deconvoluted before quantification. Absorption correction was performed in thick areas of the nanotubes by taking into account the thickness of the NTs at the analyzed position. EDS quantification was achieved by using the Brown-Powell model for the ionization cross-sections. This set-up allows to capture in a quantitative manner the ratios of La, Ta and Nb although the precise quantification of light elements such as sulfur is not certain. Most of the SR-EELS spectra were acquired with an energy dispersion of 1.0 eV/pixel and the acquisition time was about 0.2 second/pixel. The convergence and collection angles were 21 and 16 mrad, respectively. The EELS spectra were acquired in Dual EELS mode allowing the simultaneous acquisition of the La- $M_{4,5}$ , Ta- $M_{4,5}$  and Nb- $L_{2,3}$  edges situated at 830, 1750 and 2370 eV, respectively. The low-energy range of the CCD was used to acquire the La- $M_{4,5}$  and Ta- $M_{4,5}$  edges while the high-energy range was used to acquire the Ta- $M_{4,5}$  and Nb- $L_{2,3}$  edges. The two spectra were then spliced after acquisition to perform the simultaneous quantification of the three edges of interest. EELS datasets were processed by using the Digital Micrograph and Hyperspy softwares.<sup>31</sup> The most representative spectra were submitted to the open-access EELS Database as references.<sup>32</sup> HRSTEM imaging was performed by using high-angle annular dark-field

(HAADF), annular dark-field (ADF) and annular bright field (ABF) detectors. The inner and outer angles for HAADF, ADF and ABF imaging were 100 and 200 mrad, 24 and 134 mrad, 13 and 133 mrad respectively. Integrated differential phase contrast (iDPC) imaging was performed by using a four quadrants detector with inner and outer angles of 12 and 68 mrad, respectively.<sup>33</sup>

#### X-ray diffraction

The crystallographic structure of the MLCs was investigated by XRD (Rigaku, model TTRAX III) theta-theta diffractometer equipped with a rotating copper anode ( $\lambda=1.5406 \text{ \AA}$ ) operating at 50 kV and 200 mA and with a scintillation detector. An asymmetric  $2\theta$  scan with a fixed incident angle at 2 degree was performed using nearly parallel x-ray beam focused by a cross beam optical (CBO, Rigaku) attachment. Qualitative phase analysis was performed using the Jade 2010 software (Materials Data, Inc) and PDF-4+ 2017 database (ICDD). Unfortunately, the powders analyzed by the XRD study were heavily oxidized, due either to beam induced oxidation or improper handling of the material. Nevertheless several important conclusions were drawn from this analysis, which are discussed below.

#### Raman spectroscopy

Raman measurements from 100 to 500  $\text{cm}^{-1}$  were recorded on individual nanotubes using the back-reflection mode. The LabRAM HR Evolution (HORIBA, France) set-up with a 633 nm laser and 2 mW maximum power on the sample was used. The instrument is equipped with an 800 mm spectrograph allowing for a very high spectral resolution and low stray light. The pixel resolution is  $\sim 1.8 \text{ cm}^{-1}$  when working with a 600 gr/mm grating and a 532 nm laser. The sample was illuminated using several microscope objectives, such as x100 objective (MPlanFL NA=0.9, Olympus, Japan). The Raman spectra were measured using a 1024  $\times$  256 pixel open electrode front-illuminated CCD camera cooled to  $-60 \text{ }^\circ\text{C}$  (Syncerity, HORIBA, USA). The system utilizes an open confocal microscope (Olympus BXFM) with a spatial resolution better than 1  $\mu\text{m}$ . The measurements were obtained with the laser beam focused on individual nanotubes.

## RESULTS AND DISCUSSION

**Figure 2** shows a series of typical SEM pictures of the synthesized nanotubular material for different Nb concentrations. It can be observed that with ascending Nb content (and proportionally descending Ta concentrations) in the reaction mixture, the number of nanotubes goes down. While for 10 at% Nb, the abundance of the nanotubes is as high as 20%, the concentration of nanotubes descends with increasing Nb content in the reaction mixture, but not in a linear way, as displayed in **Figure 3a** (red curve). Semi-quantitative chemical analysis was carried-out using EDS/TEM to determine the niobium content in the nanotubes, which is also displayed in **Figure 3a** (black curve). This analysis shows that the Nb content in the tube-lattice increased very slowly up to 40 at% of Nb in the reaction mixture, and subsequently was sharply increased. Consequently, the yield of the nanotubes in the reaction mixtures decreased with increasing niobium content in

the reaction mixture with concomitant increasing Nb content in the nanotubes.

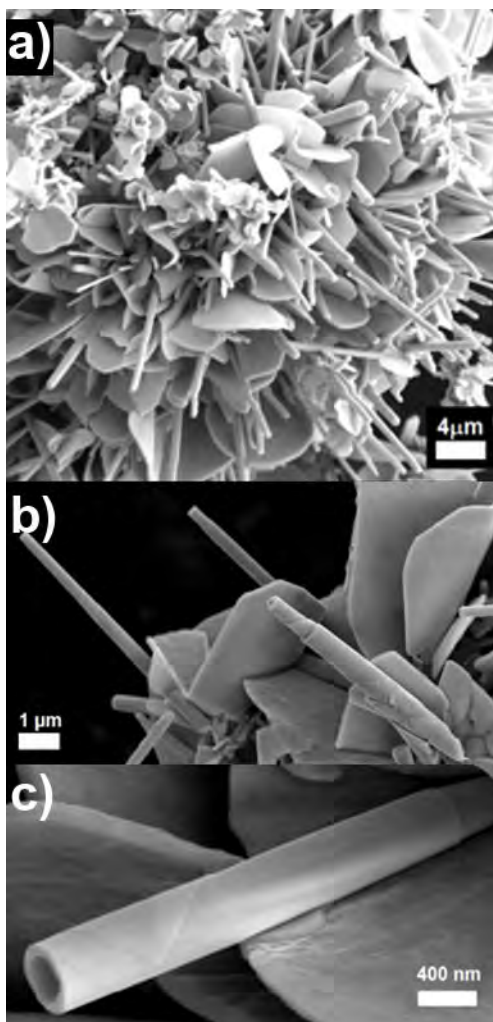


**Figure 2.** SEM micrographs of tubes from  $(\text{LaS})_{1.15}\text{Nb}_x\text{Ta}_{(1-x)}$  with a) 10 at%; b) 60 at% and c) 80 at% of Nb, i.e. 90 at%, 40 at% and 20 at%, of tantalum, respectively, added to the reaction mixture.

**Figure 3b** reports the ratio between lanthanum and niobium in the nanotubes, obtained via semi-quantitative EDS/TEM analysis of the tubes. Formally, the ratio between the two sulfides is determined by the relation  $2(a_{\text{TaS}_2}/a_{\text{LaS}})$ . Therefore, the composition of (bulk) MLCs are:  $(\text{LaS})_{1.15}\text{TaS}_2$ <sup>23</sup> and  $(\text{LaS})_{1.14}\text{NbS}_2$ <sup>24,34</sup> respectively. The reported  $\text{La}/(\text{Nb}+\text{Ta})$  ratio in the  $(\text{LaS})_{1.15}\text{Nb}_x\text{Ta}_{(1-x)}$  nanotubes increased with increasing Nb concentration. Up to 60% at% Nb in the precursor mixture, this ratio did not exceed the expected 1.15 ratio. However, from 60 at% and onwards this ratio increased substantially and reaches the unphysical value of 2 at 90 at% Nb. As it will be shown later, the sample with 80% Nb in the precursor shows three distinct groups of nanotubes with different values of  $\text{La}/(\text{Nb}+\text{Ta})$  ratios. Furthermore, as also discussed below the composition of the nanotubes with high Nb-content (above 60 at% Nb in the precursor) is not constant in the radial and axial direction, which makes the EDS/TEM

analysis presented in **Figure 3b** inaccurate at high (> 60 at%) Nb content of the precursor. This complex picture cannot be described by averaged values, as explained below. Nevertheless, the overall trend of increasing Nb content and  $\text{La}/(\text{Nb}+\text{Ta})$  ratio in the nanotubes with higher Nb content in the precursor, is correct.

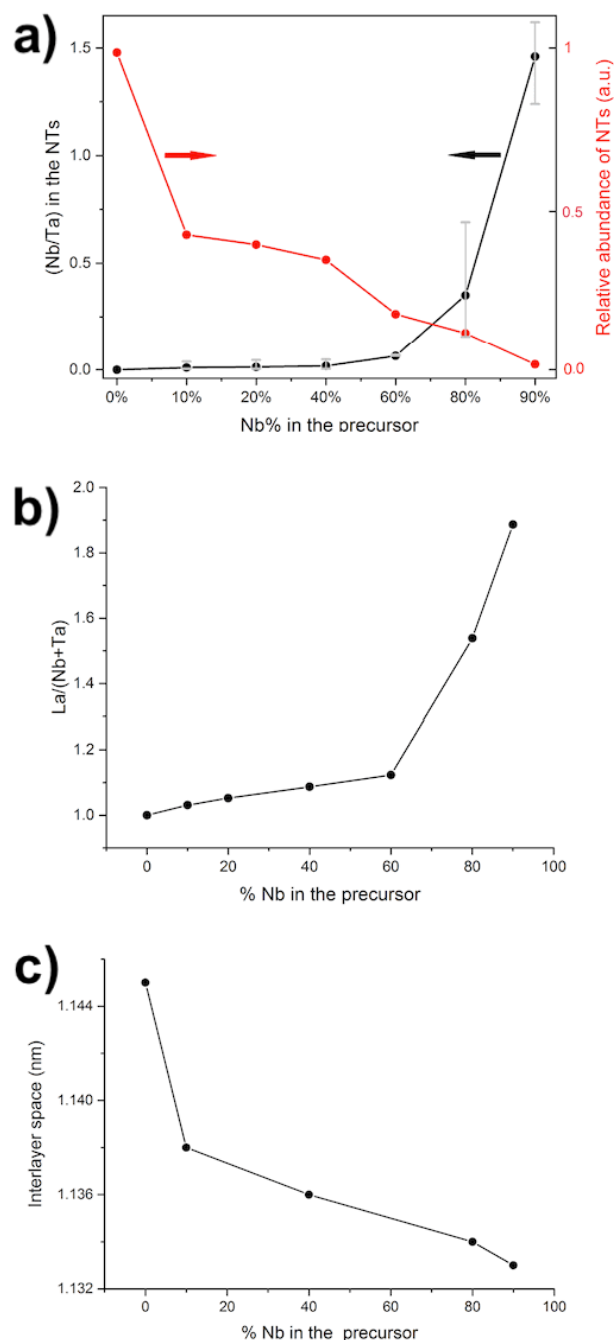


**Figure 3.** a) The Nb/Ta content ratio (black curve) (analyzed by TEM/EDS) and the relative abundance of nanotubes in  $\text{LaS-Nb}_x\text{Ta}_{(1-x)}$  (red curve-measured by analyzing the SEM data) as a function of Nb at% in the precursor mixture. b) The ratio between the at% of  $\text{La}/(\text{Nb}+\text{Ta})$  in the mixed  $\text{LaS-Nb}_x\text{Ta}_{(1-x)}$  tubes as a function of the formal at% of Nb in the precursor. c) The

interlayer spacing ( $c/2$ ) of the  $\text{LaS-Nb}_x\text{Ta}_{(1-x)}$  nanotubes as a function of the Nb content (at%) in the precursor's mixture.

**Figure 3c** shows the interlayer spacing in the  $(\text{LaS})_{1.15}\text{Nb}_x\text{Ta}_{(1-x)}$  nanotubes as a function of the formal Nb at% concentration in the precursor. The interlayer spacing was determined from the intensity profile obtained with the TEM (see **Figure 4**). The precision of the determination of lattice spacing by HRTEM is about 10 pm. The two main sources of error are the lens hysteresis, which affects the reproducibility of the magnification, and the magnification anisotropy, which affects lattice spacing measured in different directions. Both errors are in the order of 0.5-1%. The interlayer spacing drops first from 1.144 nm for pure  $\text{LaS-TaS}_2$  tubes to 1.138 (10 at% Nb) and then to 1.133 nm for 90 at% Nb. These values are somewhat smaller than the values reported for bulk  $\text{LaS-TaS}_2$  (1.152 nm)<sup>26</sup> and  $\text{LaS-NbS}_2$  (1.151 nm).<sup>24</sup> The ionic radius of  $\text{Ta}^{4+}$  (82 pm) is the same as that of  $\text{Nb}^{4+}$  ions.<sup>35</sup> It is well known that Ln-based MLC gain some extra stability through charge transfer from the  $\text{Ln}^{2+}$  to the  $\text{Ta}^{4+}$ .<sup>22</sup> Therefore, the size of  $\text{Ta}^{3+}$  (86 pm) and  $\text{Nb}^{3+}$  (86 pm)<sup>35</sup> were considered as well. Thus, the ionic radii do not seem to play a role in the interlayer spacing. Clearly though, the sulfides of Ta and Nb are not purely ionic. In fact, the Nb-S bond in the  $\text{NbS}_2$  lattice is 82% covalent,<sup>27</sup> i.e. somewhat larger than that of the Ta-S bond (78%). The interlayer ( $c/2$ ) distance of  $2\text{H-TaS}_2$  (6.05 Å) and  $2\text{H-NbS}_2$  (5.94 Å), represents a 1.8% contraction in the interlayer lattice spacing.<sup>36</sup> Therefore, the 1% contraction of the interlayer spacing ( $c/2$ ) with increasing Nb content in the  $\text{LaS-Nb}_x\text{Ta}_{(1-x)}\text{S}_2$  nanotubes is comparable with the variation of the interlayer spacing of the binary  $\text{TaS}_2$  and  $\text{NbS}_2$  compounds.

TEM analysis of the  $\text{LaS-Nb}_x\text{Ta}_{(1-x)}\text{S}_2$  tubes was undertaken. The outer layers of a few such nanotubes with various Nb content are shown in **Figure 4**. Since the tubes had diameter of 200 nm, the study was limited to the outer surface layers of these tubes. Nevertheless, these images demonstrate that the structure of these MLC tubes is relatively well preserved. However, the outer surface of the tube (**Figures 4a** and **4b**) has degraded. The outermost crystalline layer of the tube is  $\text{Nb}_x\text{Ta}_{(1-x)}\text{S}_2$  and the MS-TS<sub>2</sub> superstructure is also clearly visible. The ED pattern of  $\text{LaS-TaS}_2$  tubes indicate much disorder in the stacking of the layers<sup>22</sup> and their reduced crystalline quality compared to the bulk materials. Indeed, the diffraction spots are quite streaked and faint, which attest to the relatively poor crystallinity of the tube. **Figures S1a** and **b** show the nanobeam ED pattern in STEM mode of the nanotubes with 20 at% and 40 at% Nb content in the precursor. The ED was taken with the STEM probe of 3 nm diameter focused on the central part of the tubes and hence the diffraction from the  $c$ -axis is absent. The absence of 6-fold and 4-fold periodicity for the hexagonal and rocksalt sublattices in **Figure S1a** is attesting to the poor crystallinity of the specific 20 at% tube, which is quite surprising given the good yield and apparently good crystallinity reflected from the SEM images (not shown). On the other hand, **Figure S1b** displays two sets of hexagonal patterns of the  $\text{Nb}_x\text{Ta}_{(1-x)}\text{S}_2$  sublattice which shows that it accommodates two orientations in the tube. The splintering of the diffraction spots into pairs is reminiscent of the small chiral angle of the tube ( $\sim 3^\circ$ ). The nanobeam ED pattern of a nanotube prepared from 80 at% niobium in the precursor is shown in

**Figure S1c**. The ED reveals that in contrast to many MLC tubular structures, the growth axis of the tube does not coincide with the  $b$ -axis of the  $\text{Nb}_x\text{Ta}_{(1-x)}\text{S}_2$  (10.0) and that of the  $\text{LaS}$  (020). Similar ED patterns are described in **Figure S1** of the SI of Ref. 37. The schematic model describing the relative orientation of the different layers with respect to the growth axis is shown in **Figure S3b** of this work.<sup>37</sup> The ED displayed in **Figure 4c** is further discussed below.

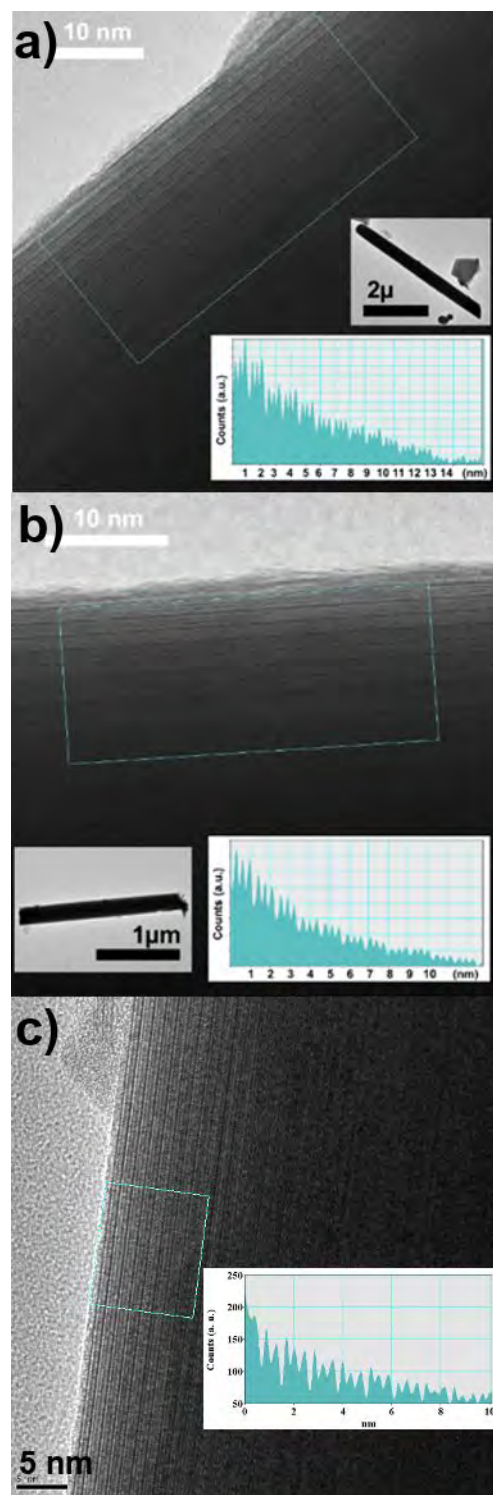


**Figure 4.** TEM micrograph of typical  $\text{LaS-Nb}_x\text{Ta}_{(1-x)}\text{S}_2$  tubes

with different Nb content in the precursor: a. 10 at%; b. 40  
at%, c. 80%.

1  
2  
3  
4  
5  
6  
7  
8  
9  
10  
11  
12  
13  
14  
15  
16  
17  
18  
19  
20  
21  
22  
23  
24  
25  
26  
27  
28  
29  
30  
31  
32  
33  
34  
35  
36  
37  
38  
39  
40  
41  
42  
43  
44  
45  
46  
47  
48  
49  
50  
51  
52  
53  
54  
55  
56  
57  
58  
59  
60

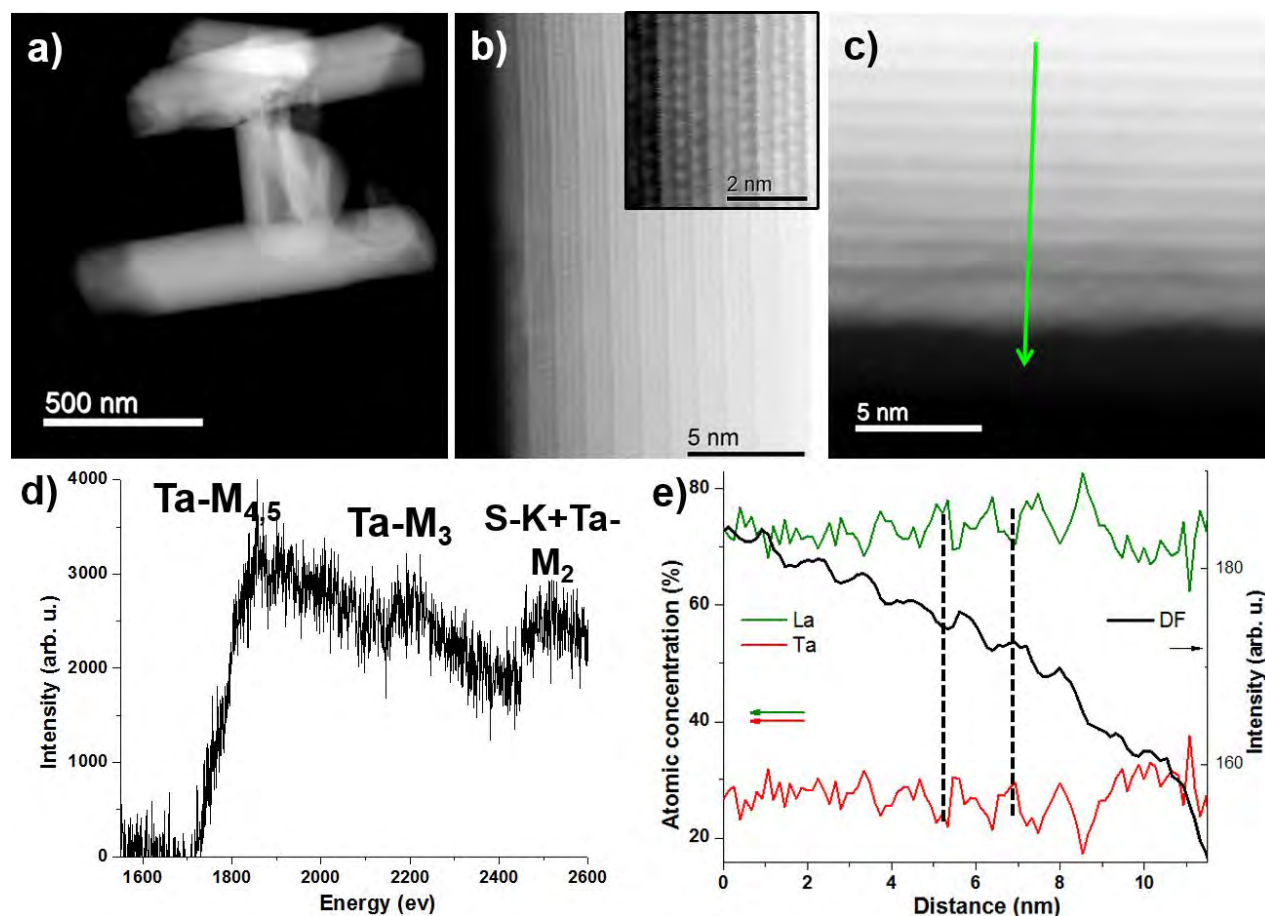


**Figure 5.** a) STEM HAADF micrograph of the NTs synthesized with 40 at% of Nb content in the precursor. b) HRSTEM HAADF micrograph of one of the NT shown in **Figure 5a**. The inset shows a magnified view. c) STEM ADF micrograph. The green arrow highlights the area used to perform the EELS analysis. d) Corresponding EELS spectra showing the Ta-M and S-K edges. e) Atomic concentration of La and Ta superposed with the intensity profile of the dark field image. The dotted lines highlight two areas with low and high intensity in the dark field image.

Given the heavy oxidation of the tested phases, only few conclusions could be drawn from the XRD analysis. It should be recalled that even for 10 at% Nb, the nanotubes phase makes a very small fraction (ca. 30%) of the total material and less so in the higher Nb-content phases analyzed here. The interlayer  $c/2$ -distance of 2H-TaS<sub>2</sub> (6.05 Å) is appreciably larger than that of 2H-NbS<sub>2</sub> (5.94 Å).<sup>36</sup> On the other hand as stated above, the interlayer spacing of bulk MLC LaS-TaS<sub>2</sub> (1.153 nm)<sup>26</sup> is only slightly larger than that of LaS-NbS<sub>2</sub> (1.152 nm).<sup>24</sup> Therefore, the 7.767° peak in the XRD analysis represents the (0002) or  $c/2$  of the respective bulk MLC material. In agreement with the interlayer spacing of the two pure compounds, this peak (and its higher harmonics) shows little shift only upon increasing the Nb content (and reducing the Ta content).

HRSTEM analyses were also performed on nanotubes synthesized with 40 at% Nb content in the precursor (**Figure 5**). This sample presents few nanotubes with a high crystalline

quality. All the observed nanotubes show a normal periodicity (**Figure 5b**). Depending on the probed nanotube, the interlayer spacing was found to vary between 1.07 and 1.20 nm. It should be noted that the Nb-L<sub>3</sub> edge cannot be highlighted in the EELS spectrum suggesting that the concentration of Nb in these nanotubes is below a few percent (**Figure 5d**). As a consequence, the interpretation of the contrast in the HRSTEM HAADF images is more straightforward than for the nanotubes synthesized with higher concentration of Nb as discussed below: the highest and lowest intensity features corresponding to the Ta (Nb) and La sub-system, respectively (**Figure 5e**). Note that, as expected, the Ta and La are in antiphase with respect to each other, which is a manifestation of the superlattice of LaS and Nb<sub>x</sub>Ta<sub>(1-x)</sub>S<sub>2</sub> layers in the tube. The top surface of the nanotube is coated with a poorly crystalline (amorphous) film. This film has an ill-defined chemical composition, consisting of La and Ta oxides as revealed by EELS analyses (not shown here). Beneath the amorphous film, a well resolved crystalline superstructure (inset of **Figure 5b**) with Nb<sub>x</sub>Ta<sub>(1-x)</sub>S<sub>2</sub> as the outermost layer of the tube, is resolved.

To understand the variation of the La/(Nb+Ta) ratio for the nanotubes synthesized with 80% of Nb in the precursor, a detailed STEM analysis was performed for these nanotubes. It was found that the nanotubes synthesized with 80% of Nb in the precursor can be divided into three groups: NTs with a normal periodicity; nanotubes showing a juxtaposition of the normal and double periodicity and nanotubes displaying purely a double periodicity.

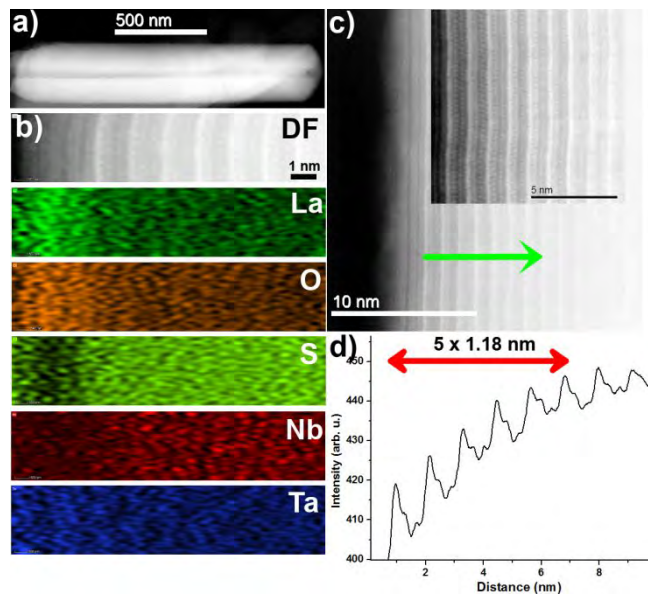


**Figure 6.** a) Low-magnification STEM-ADF micrograph of one  $\text{LaS-Nb}_x\text{Ta}_{(1-x)}\text{S}_2$  tube synthesized with 80 at% of Nb content in the precursor. b) HRSTEM-ADF micrograph of the surface of the NT. The inset shows a magnified image of the filtered image. c) (from top to bottom) : HRSTEM image, La, S, Nb and Ta chemical maps (in at%) extracted from EDS spectrum image. d) Intensity profile extracted from the area highlighted by the green arrow shown in b).

About 4/10 of the nanotubes observed by HRSTEM presented a normal periodicity. **Figure 6** displays the STEM analysis performed on the nanotubes synthesized with 80 at% Nb and showing a simple periodicity. This nanotube has a length of 1.7  $\mu\text{m}$  and external and internal diameters of 325 and 65 nm, respectively. This nanotube presents a high crystalline quality as it can be seen in the HRSTEM ADF micrograph (**Figures 6b** and **6c**). The periodicity of this NT is about 1.18 nm and the alternating system of bright and dark layers, corresponding to the  $\text{Nb}_x\text{Ta}_{(1-x)}\text{S}_2$  and the LaS sub-systems, respectively, is clearly highlighted in the HRSTEM micrograph and in the corresponding intensity profile (**Figure 6d**). The values of the *c*-axis periodicity determined with the HRSTEM were systematically higher than those observed with the TEM (**Figure 3c**). This discrepancy could be a manifestation of the variability among the batches of the synthesized material, or could emanate from a systematic calibration error in the microscopes. The first layers of the  $\text{Nb}_x\text{Ta}_{(1-x)}\text{S}_2$  sub-system

seems to follow the *1T* crystallographic structure (**Figure S2**),<sup>38</sup> which is quite unusual in view of the state of the art.<sup>37</sup> It should be noted that the same behavior has been observed for nearly all the NTs synthesized with 80% of Nb, independently of their periodicity. The results of the EDS quantification are shown in **Table S1**. At the center of the nanotube, there is an equal proportion of Nb and Ta and the La/(Nb+Ta) ratio is also close to unity. While approaching the surface, a slight increase of the at% of Ta and a slight decrease of the at% of Nb takes place which results in a Nb/Ta ratio close to 0.7). The value of the La/(Nb+Ta) ratio close to the surface is about 0.9. At the outermost layers of the nanotube near the surface, a strong increase of the at% of La and O as well as a strong decrease of the at% of S and Nb can be observed in the corresponding EDS chemical maps (**Figure 6c**). The detailed quantification of this area is reported in **Figure S3**. The at% of La reaches nearly 60% and, as a consequence, the La/(Nb+Ta) ratio increases up to about 2.7. These chemical inhomogeneities at the outermost layers near the nanotube surface could explain the unphysical value of the La/(Nb+Ta) ratio reported in **Figure 3b** for nanotubes synthesized with 80% of Nb, or more, in the precursor. It also reflects the strong oxidation of the nanotube surface, which is visible also in **Figures 6b** and **6c**.

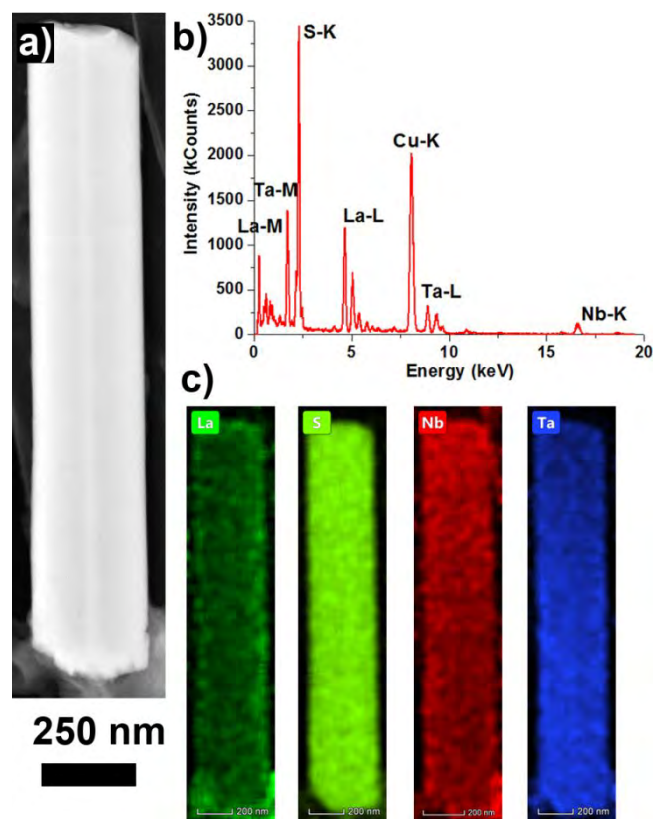


**Figure 7.** a) Low-magnification STEM-ADF micrograph of  $\text{LaS-Nb}_x\text{Ta}_{(1-x)}\text{S}_2$  tube with 80 at% of Nb content in the precursor exhibiting both normal (1.12) and double (2.25 nm) LaS-TaS<sub>2</sub> periodicity. b) EDS spectrum acquired on the NT.

C) EDS chemical maps at% of S, La, Nb and Ta (from left to right).

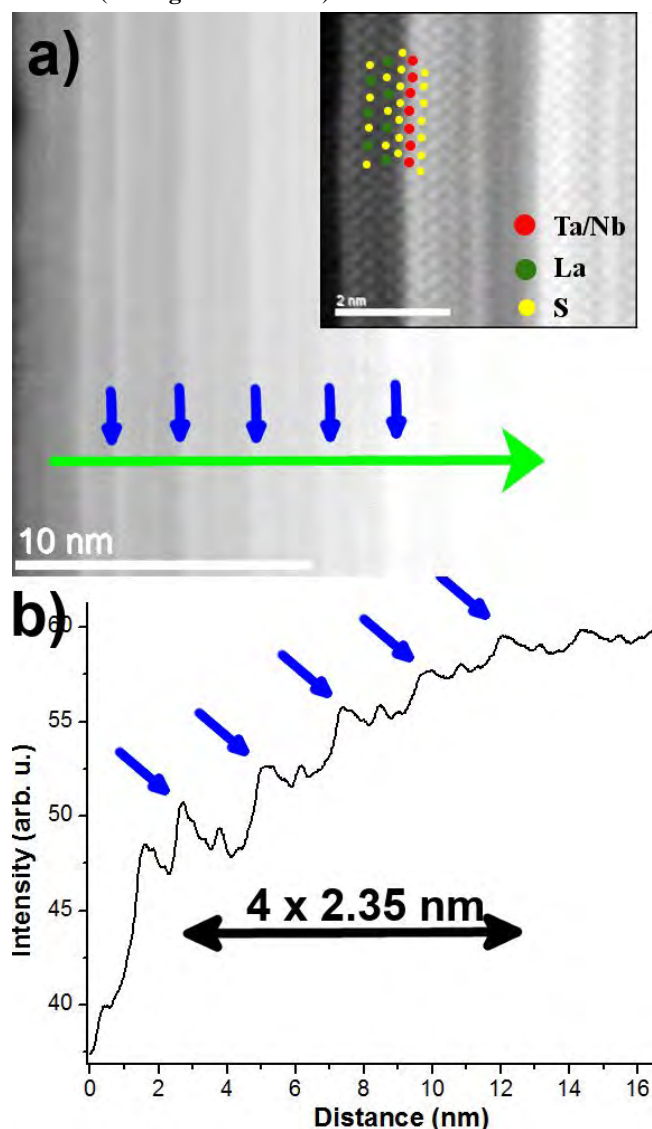
**Figure 7a** shows a low-magnification STEM ADF micrograph of another kind of  $\text{LaS-Nb}_x\text{Ta}_{(1-x)}\text{S}_2$  tube present in the sample synthesized with 80 at% of Nb content in the precursor. As it will be discussed below, this nanotube showed a juxtaposition of normal (1.12 nm) and double (2.25 nm) periodicity. About 2/10 of the nanotubes observed by HRSTEM showed the juxtaposition of the normal and double periodicity. This nanotube has a length of 1.9  $\mu\text{m}$  and external and internal diameters of 335 and 70 nm, respectively. Note however that the outer diameter of the nanotube at the top is smaller somewhat from that in the bottom: 330 and 340 nm at the top and at the bottom, respectively. A typical EDS spectrum acquired at the center of this NT is shown in **Figure 7b**. From the EDS spectrum image, the at% chemical maps of S, La, Nb and Ta were extracted and are shown in **Figure 7c**. Note that, whereas La and S are homogeneously distributed inside the NT, the Nb and Ta maps show clearly a chemical gradient along the long axis of the NT. The Nb and Ta maps are anti-correlated; the Nb content is higher at the top part of the image whereas the Ta content is higher in the bottom of the image. The same trend has been confirmed when using the 4-windowless EDS detectors separately, which rules out the influence of geometrical effects on these chemical maps.<sup>39</sup> Since the vapor pressure of  $\text{TaCl}_5$  is higher than that of  $\text{NbCl}_5$ ,<sup>40</sup> it is suggested that the lower side of the imaged nanotube is indeed the root, while its upper side presents the top of the grown nanotube. The details of the growth mechanism of  $\text{LaS-TaS}_2$  nanotubes has not been resolved as yet. However, by following the time dependence of the growth (to be published), it was observed that after formation of the short tubes in the root in the early stage of the growth, they continue to grow for a few hours to their final length. Therefore, the volatility of the metal halides is a prime parameter determining the composition of the nanotube as shown in the above analysis. Since the interlayer spacing of  $\text{LaS-TaS}_2$ <sup>27</sup> is somewhat larger than that of  $\text{LaS-NbS}_2$ ,<sup>24</sup> it would be expected that the Nb-rich top of the nanotube is smaller than the Ta-rich bottom part, as is indeed the case. Also, in conformity with the analysis of the nanotube with simple periodicity (**Figure 6**) some enrichment of the surface with respect to La is clearly noticed.

**Figure S4** gives the detailed results of the EDS quantification performed in various areas of this NT (shown also in **Figure 7**). Along the long axis, the Nb/Ta ratio shows large variations, decreasing from 3.40 (position 1 top-center) to 0.73 (position 5 bottom-center). Again, the lower vapor pressure of  $\text{NbCl}_5$  compared to that of  $\text{TaCl}_5$ ,<sup>40</sup> suggests that the root of the tube is in the lower part of the image (5), whereas point 1 represents the termination of the nanotube growth. The  $\text{La}/(\text{Nb}+\text{Ta})$  ratio decreases from 0.92 in the bottom (5) to 0.70 in the top reflecting the enrichment of Nb in the NT lattice with the nanotube growth. In the center of the NT, the Nb content is nearly equal to the Ta content. However, an increase of the atomic concentrations of Nb and La can be observed towards the surface of the NT.

**Figure 8** shows a HRSTEM ADF micrograph acquired at the surface of the NT analyzed in **Figure 7**. This NT presents a

good crystalline quality. The alternation of bright layers and dark layers spaced by 1.12 nm, corresponding to the Ta/Nb and La sub-systems respectively, can be clearly highlighted. The inset of **Figure 8a** shows the HRSTEM ADF filtered image superposed with the atomic model of the  $\text{LaS-Nb}_x\text{Ta}_{(1-x)}\text{S}_2$  tube which confirms the *1T* crystallographic structure of the  $\text{Nb}_x\text{Ta}_{(1-x)}$  sub-system. Surprisingly, a superstructure with a periodicity of about 2.25 nm can also be highlighted in the image and in the corresponding intensity profile (blue arrows in **Figures 8a** and **8b**). This superstructure corresponds to an increase in the intensity of half of the Ta/Nb layers and thus reflects an organized spatial modulation of the Ta/Nb ratio.

**Figure 9a** shows a HRSTEM ADF micrograph corresponding to the third type of  $\text{LaS-Nb}_x\text{Ta}_{(1-x)}\text{S}_2$  tube observed in the sample synthesized with 80 at% of Nb content and which presents a double periodicity in the precursor. This nanotube has a length of 3.3  $\mu\text{m}$  and an external diameter of 330 nm (inset of **Figure 9a**). Surprisingly this nanotube shows an apparent periodicity of 2.35 nm. This periodicity has been observed for about 4/10 of the nanotubes synthesized with 80% of Nb in the precursor. It should be noted that misfit nanotubes with a periodicity of about twice the normal periodicity were already reported for  $\text{CeS-TaS}_2$  NTs, but their structure was not elucidated (see **Figure S7b** there).<sup>22</sup>



1 **Figure 8.** a) HRSTEM-ADF micrograph of the surface of the  
2 NT shown in **Figure 7**. The inset shows a filtered image  
3 superposed with the atomic model of the  $\text{LaS-Nb}_x\text{Ta}_{(1-x)}\text{S}_2$   
4 tube. The green arrow highlight the area used to extract the  
5 image intensity profile shown in b. The blue arrows highlight  
6 the superstructure.  
7  
8  
9

10 **Figures 9b** and **9c** shows a HRSTEM HAADF image of the  
11 same nanotube and the corresponding intensity profile,  
12 respectively. Four layers can be distinguished between the two  
13 layers labeled X and spaced by 2.35 nm: two layers labelled z  
14 and two other layers labelled y and y'. y' layers are defined as  
15 being closer to the surface of the NT than y layers. The z layers  
16 present the lowest intensity in the HAADF image intensity  
17 profile highlighting thus a lower atomic number. On the other  
18 hand, the X, y and y' layers present similar intensities, even if  
19 the thickness variation at the surface of the nanotube hinders a  
20 detailed analysis of the intensity profile.  
21  
22  
23  
24  
25  
26  
27  
28  
29  
30  
31  
32  
33  
34  
35  
36  
37  
38  
39  
40  
41  
42  
43  
44  
45  
46  
47  
48  
49  
50  
51  
52  
53  
54  
55  
56  
57  
58  
59  
60

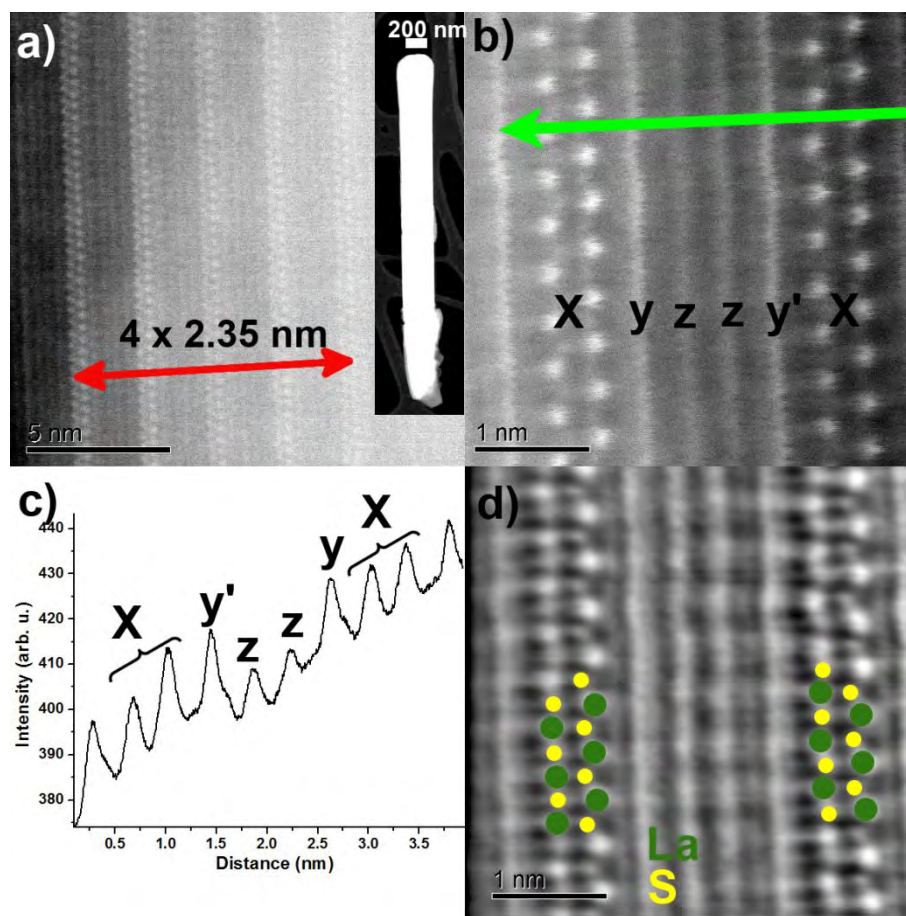


**Figure 9.** a) HRSTEM-ADF micrograph of the surface of the NT shown in the inset. b) HRSTEM-HAADF micrograph taken on the other side of the NT. The green arrow highlight the area used to extract the c) image intensity profile. d) iDPC image acquired simultaneously with the HAADF image shown in b) and superposed with the atomic model of the LaS sub-system.

To get deeper insight, iDPC micrographs acquired simultaneously with the HAADF micrographs were also analyzed. iDPC is a powerful technique to locate, in the same image, light and heavy columns with high precision.<sup>33,41</sup> The direct imaging of sulfur atoms in a misfit nanotube is delicate due to the intrinsic tubular structure,<sup>22</sup> and despite the many TEM studies undertaken on these compounds, it has never been reported before. **Figure 9d** shows the iDPC micrograph taken at the surface of the NT. The S atoms are clearly imaged for the X layers and the distorted rock-salt structure of the LaS sub-system can be easily identified. However, no more structural information is highlighted for the remaining layers.

To get more insight on the chemical nature of these layers, SR-EELS studies have been performed at the surface of the NT (**Figure 10**). The La-M<sub>4,5</sub>, Ta-M<sub>4,5</sub> and Nb-L<sub>3</sub> edges can be clearly identified at 830, 1750 and 2370 eV (**Figure 10b**), respectively. It should be noted that the broad peak situated at 2450 eV corresponds to an overlap of the Nb-L<sub>2</sub>, S-K and Ta-M<sub>2</sub> edges. From the EELS spectrum image, the La, Ta and Nb chemical maps have been extracted and are shown in **Figure 10c**. The correlation of the Ta and Nb chemical maps are clearly

highlighted as well as the anti-correlation with the La chemical map. This is a direct confirmation that the Nb atoms incorporate into the Ta (hexagonal) sub-system. Surprisingly, these chemical maps show a periodicity of about 1.3 nm showing therefore that the 2.35 periodicity nm observed in the HRSTEM images is only apparent. To get more insight on this point, the intensity profiles of the atomic concentrations have been calculated and are superposed on the ADF image acquired simultaneously with the EELS spectrum image (**Figure 10d**). It should be noted that proper quantification by EELS spectroscopy is not straightforward.<sup>42</sup> Another approach, which has already been successfully applied to the study of misfit nanotubes, is to combine chemical and spatial variations in order to determine the chemical structure at the local scale.<sup>43–46</sup> From **Figure 10d**, it can be seen that the X layers are rich in La, confirming thus that they can be ascribed to the LaS rock-salt sub-system as shown by the iDPC images. Surprisingly, the z layers are also La rich, which is in good agreement with the decrease of intensity observed in the intensity profile of the HRSTEM HAADF image with respect to the intensity of the y and y' layers. The distinct contrasts and features shown in the HRSTEM micrographs for the z and X layer can be explained

by the fact that the two LaS layers in  $z$  and  $X$  are positioned in different orientations.

1  
2  
3  
4  
5  
6  
7  
8  
9  
10  
11  
12  
13  
14  
15  
16  
17  
18  
19  
20  
21  
22  
23  
24  
25  
26  
27  
28  
29  
30  
31  
32  
33  
34  
35  
36  
37  
38  
39  
40  
41  
42  
43  
44  
45  
46  
47  
48  
49  
50  
51  
52  
53  
54  
55  
56  
57  
58  
59  
60

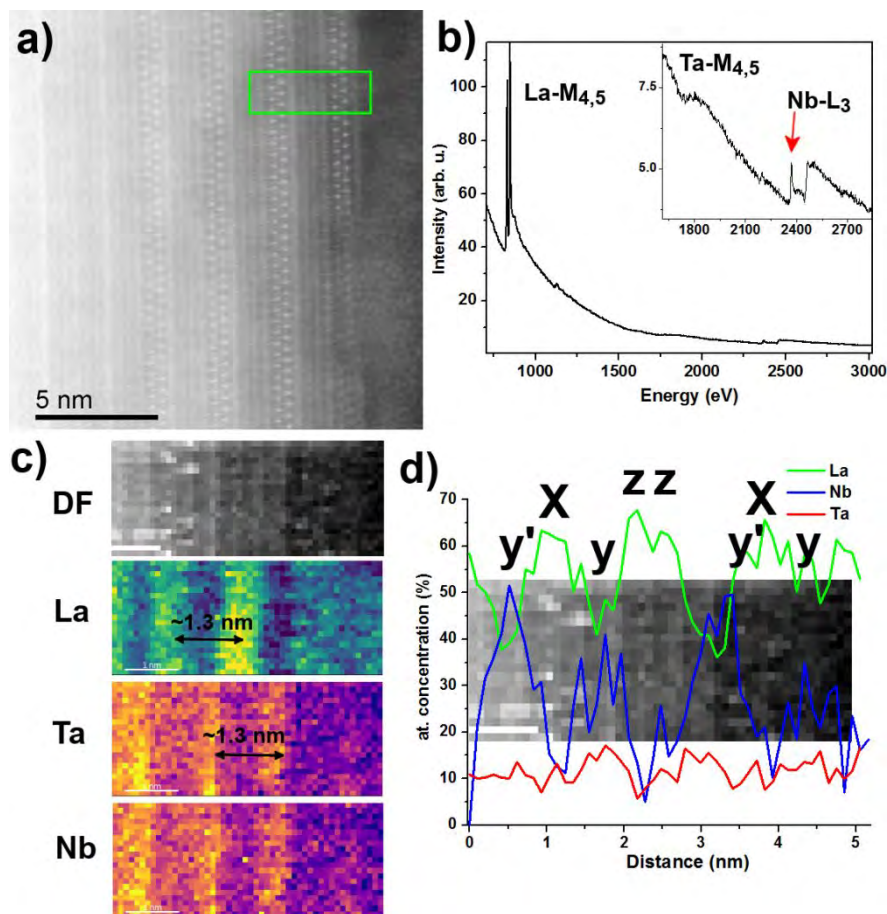


**Figure 10.** a) HRSTEM-ADF micrograph of the NT shown in **Figure 8**. The green square highlights the area used for the acquisition of the EELS spectrum image. c) Corresponding spliced EELS spectra showing the La-M<sub>4,5</sub>, Ta-M<sub>4,5</sub> and Nb-L<sub>3</sub> edges. c) (from top to bottom): dark field image acquired simultaneously with the EELS spectrum image. La, Ta and Nb chemical maps extracted from the integrated intensity of the corresponding edges. d) Intensity profiles of the atomic concentrations superposed on the dark field image.

This is supported by the electron diffraction shown in **Figure S1c**, where two orientations of the LaS-Nb<sub>x</sub>Ta<sub>1-x</sub>S<sub>2</sub> layers are clearly revealed. Here, the two subunits LaS and Nb<sub>x</sub>Ta<sub>1-x</sub>S<sub>2</sub> of the misfit layer are azimuthally rotated with respect to the other misfit layer by 30° (in fact 30° is equivalent to an azimuthal rotation of 60° in the ortho pseudo-hexagonal unit cell (90°-60°=30°)).<sup>37</sup> Similar rotations have been reported before for nanotubes of misfit compounds.<sup>21,22,39</sup> However, this is the first time that such azimuthally rotated alternating superstructure are clearly resolved and correctly interpreted. Therefore, this nanotube presents a complex superstructure with respect to the LaS and Nb<sub>x</sub>Ta<sub>1-x</sub>S<sub>2</sub> layers and also a superstructure of the misfit layers orientation corresponding to periodical 30° azimuthal rotation. Unfortunately though, the resolution with respect to the hexagonal Nb<sub>x</sub>Ta<sub>1-x</sub>S<sub>2</sub> lattice is not sufficient to determine if it follows the same alternating azimuthal rotation. It should be noted that the electron diffraction shown in **Figure S1c** corresponds to the tube shown in **Figure 4c**. This tube has been synthesized with 80 at% Nb in the precursor and has a normal

periodicity of 1.144 nm even if two orientations of the LaS-Nb<sub>x</sub>Ta<sub>1-x</sub>S<sub>2</sub> layers are revealed in the electron diffraction. This means that while the LaS (and possibly also the TaS<sub>2</sub>) have two orientations in some nanotubes, this tilt is ordered giving rise to double periodicity (as shown in **Figs. 9** and **10**) and in other cases (like the one shown in **Figure 4c** and in **Figure 6**) the tilted layers are not ordered in a superstructure, giving rise to a normal periodicity.

Furthermore, one LaS-Nb<sub>x</sub>Ta<sub>1-x</sub>S<sub>2</sub> is enriched with respect to Nb, while the other is enriched with Ta. The y and y' layers show the highest concentration of Nb and Ta, and can thus be ascribed to Nb<sub>x</sub>Ta<sub>(1-x)</sub> sub-system. The higher incorporation of Nb in the Ta sub-system for this NT explain why the y and y' layers present intensities similar to that of the X layers. Interestingly the y' layers present a higher atomic concentration of Nb than the y layers showing thus that this NT presents a spatial modulation of the Ta/Nb ratio.

Finally, EDS quantification was performed on several nanotubes showing an apparent periodicity of about 2.35 nm (Table S2). These nanotubes present values of Nb/Ta falling in the 1.5 - 2.9 range, which is clearly above the Nb/Ta ratio of the nanotubes showing a normal periodicity ( $\sim 0.7$ - $0.9$ ), highlighting thus the higher content of Nb in the Ta sub-system for these nanotubes. Interestingly, all the probed nanotubes show consistent values of La/(Ta+Nb) ratios close to 0.85. This is significantly lower than for the NTs showing a normal periodicity ( $\sim 1.0$ ). The nanostructure of the nanotubes showing a double periodicity might thus be a consequence of the La sub-system which must adapt itself to the higher Nb+Ta concentration.

### Raman analyses

Raman analyses of different MLC compounds and in particular nanotubes thereof were reported before.<sup>22,23,47,48</sup> In general, the Raman spectrum of LnS-TaS<sub>2</sub> MLC was divided between the range of 100-150 cm<sup>-1</sup> which was assigned to the MS lattice and the range 250-400 cm<sup>-1</sup> which is assigned to the TS<sub>2</sub> lattice.<sup>47,48</sup> Raman analysis of 2H and 3R NbS<sub>2</sub> as well as NbS<sub>2</sub> intercalated with organic amine molecules were also reported.<sup>28,49,50</sup> Raman analysis of 1T-NbS<sub>2</sub> is rather scarce.<sup>51</sup> Here, Raman analysis of the MLC tubes with different Nb content was carried-out. Figure 11 summarizes the results of this analysis.

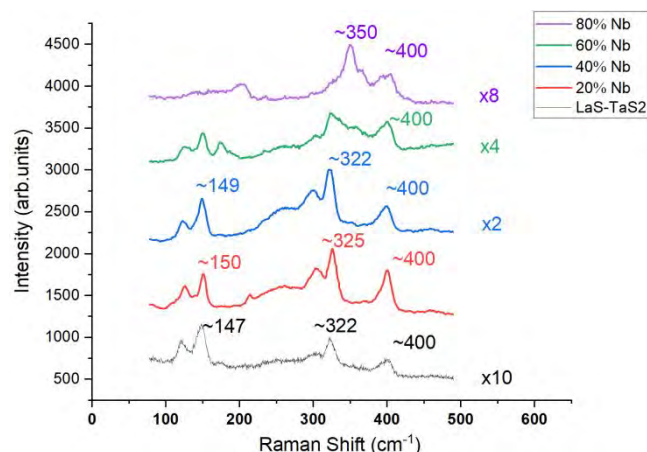


**Figure 11.** Raman spectra of five different LaS-Nb<sub>x</sub>Ta<sub>(1-x)</sub>S<sub>2</sub> MLC tubes with different Nb content.

Figs. S5-S8 provide a more extensive study of the Raman spectra of LaS-Nb<sub>x</sub>Ta<sub>(1-x)</sub>S<sub>2</sub> MLC tubes with different Nb content. Generally speaking the Raman spectra of the MLC tubes with less than 60 at% Nb content (and 40 at% Ta in the precursor), are rather uniform and reproducible. The peaks comply well with those of pure LaS-TaS<sub>2</sub> tubes with some minor shifts.<sup>8,22</sup> Above this Nb content (in the precursor mixture), the spectra (see Figs. S7 and S8) exhibit a more complex behavior. First, in both 60 and 80 at% Nb, there are noticeable differences between two groups of nanotubes. Unfortunately, it was not possible to confirm the structure of the specific nanotubes by Raman using HRTEM. In particular, the distribution of Nb atoms in the Ta sites of the TaS<sub>2</sub> and perhaps elsewhere in the nanotube lattice, could not be resolved.

Therefore, precise correlation between the Raman spectra of a given nanotube and its lattice structure is lacking.

It must be recognized, that the present MLC tubes are air-sensitive and are therefore coated by an oxide film, which is visible in the TEM analysis. These native oxides are enriched by lanthanum oxide (or oxisulfide) and are rather amorphous, and consequently their Raman peaks are likely to be rather broad and wide. The most prominent oxide modes are usually at energies above 500 cm<sup>-1</sup>, which range is not relevant to the present study.

As stated above, the Raman spectra of LnS-TaS<sub>2</sub> misfit layered compounds was divided into two main spectral ranges.<sup>47,48</sup> The low energy range around 100-150 cm<sup>-1</sup> (named RS) was associated with intralayer vibrations of the LnS lattice, while the features in the range of 250-350 cm<sup>-1</sup> were assigned to the intralayer vibrations of the hexagonal TaS<sub>2</sub> lattice. The peaks associated with the two-phonon bands of TaS<sub>2</sub> layer<sup>36</sup> in 253 cm<sup>-1</sup>, are clearly revealed.

In the present case, the Raman spectra of all the nanotubes can be also divided into the low energy modes assigned to the LaS lattice and the high frequency modes belonging to the Nb<sub>x</sub>Ta<sub>(1-x)</sub>S<sub>2</sub> lattice. The modes in the low energy range of the nanotubes produced from a precursor containing 10, 20 and 40 at% Nb can be divided into the low-energy out-of-phase vibration (RSI) of the LaS lattice at 125 cm<sup>-1</sup> and the higher energy (in-phase) phonon (RSII) in 150 cm<sup>-1</sup>.<sup>47</sup> The Raman spectra of nanotubes prepared from precursors with 60 and 80 at% Nb can be also divided into the low frequency modes belonging to the LaS lattice and the high frequency modes associated with the Nb<sub>x</sub>Ta<sub>(1-x)</sub>S<sub>2</sub> lattice. However, the LaS (low energy modes) of the nanotubes prepared from 60 at% Nb exhibit an extra peak at 170 cm<sup>-1</sup>. The Raman spectra of the nanotubes prepared from 80 at% Nb (low energy range) show a broad peak at 200 cm<sup>-1</sup>. Since the HRTEM did not give any indication for inclusion of Nb atoms in the LaS lattice, these higher energy peaks could be assigned to the in-phase vibration of the LaS. However, the origin of the blueshift of this peak in nanotubes with higher Nb content is not clear.

The 400 cm<sup>-1</sup> transition was assigned to the A<sub>1g</sub> vibration of the 2H-TaS<sub>2</sub>.<sup>47</sup> This transition is characterized by symmetric vibrations of the sulfur atoms along the *c*-axis, and the metal atom remains static. The A<sub>1g</sub> mode of 2H-NbS<sub>2</sub> appears at a lower energy (380 cm<sup>-1</sup>)<sup>27</sup> compared to 2H-TaS<sub>2</sub> (400 cm<sup>-1</sup>). This is a manifestation of the weaker spring constant for the S-metal bond for the lighter Nb compared with the heavier Ta atom. In contrast to other transitions, this mode did not show any shift with variation of the Ln atom.<sup>24,34</sup> Here too, the position of this peak remains unchanged with increasing Nb (and reducing Ta) content. However, in nanotubes prepared from the 60 and especially the 80 at% enriched Nb, the 400 cm<sup>-1</sup> (A<sub>1g</sub>) transition is convoluted with a second peak appearing at an energy close to 385 cm<sup>-1</sup>, which is consistent with the E<sub>2g</sub> transition in 2H-NbS<sub>2</sub>.<sup>28</sup> Furthermore, a detailed Raman study of 2H-NbS<sub>2</sub><sup>48</sup> concluded that the A<sub>1g</sub> peak is at 363 cm<sup>-1</sup>. Indeed the MLC tubes prepared with 60 and 80 at% niobium exhibit a similar peak (see Figure 11). The fact that both the 363 and 400

$\text{cm}^{-1}$  ( $A_{1g}$ ) peaks appear in the spectra of a single tube entails that, most likely, the Nb distribution is not uniform within the nanotubes, some regions (layers) are enriched with Nb while others with Ta. This confirms the HRSTEM (EDS) findings showed and discussed above.

2H-TaS<sub>2</sub> exhibits incommensurate charge density wave (CDW) transition at room temperature. Raman spectra of this compound as a function of temperature was reported before.<sup>52,53</sup> These measurements showed that the 400  $\text{cm}^{-1}$  ( $A_{1g}$ ) peak disappears below 375 K, i.e. at the outset of the incommensurate CDW phase. Thus, it is surmised that a CDW transition does not occur at the MLC LaS-Nb<sub>x</sub>Ta<sub>(1-x)</sub>S<sub>2</sub> tubes. A Raman study of pure and (ethylene diamine-EDA) intercalated 2H-TaS<sub>2</sub> were reported as well (most likely, the 2H-TaS<sub>2</sub> was a metastable phase in this study).<sup>54</sup> The authors concluded that the CDW transitions in 2H-TaS<sub>2</sub> are greatly suppressed by the intercalation of electron donors, like amines. One may regard the MLC of the type MS-TS<sub>2</sub>, including the LaS-Nb<sub>x</sub>Ta<sub>(1-x)</sub>S<sub>2</sub>, as an intercalation compound where a layer of LnS is inserted in between each two layers of the hexagonal TS<sub>2</sub> lattice (Nb<sub>x</sub>Ta<sub>(1-x)</sub>S<sub>2</sub> in this case). The LnS donates an electron to the Nb<sub>x</sub>Ta<sub>(1-x)</sub>S<sub>2</sub> leading to a partial filling of the  $d_{z^2}$  level of the metal. Presumably, this process suppresses the semimetallic character of the TS<sub>2</sub> layer and consequently, its tendency to undergo a CDW transition, but no direct evidence to this effect is reported here.

Previously, the shift of the  $E_{2g}$  line to higher energies of the LnS-TS<sub>2</sub> MLC (compared to the pure TS<sub>2</sub> compound) was attributed to a charge transfer from the LnS lattice to the TS<sub>2</sub> lattice.<sup>22,37,47,48</sup> In the present study, a clear shift of this peak to higher energies from 322  $\text{cm}^{-1}$  for pure LaS-TaS<sub>2</sub> nanotubes to 350  $\text{cm}^{-1}$  for the Nb-enriched (60 and 80 at% Nb) is observed. In the present work four nanotubes from the 60 and 80 at% Nb enriched phases, were analyzed. Thus, one (out of four) LaS-Nb<sub>x</sub>Ta<sub>(1-x)</sub>S<sub>2</sub>, of the 60 at% Nb and three (out of four) nanotubes prepared from 80 at% Nb exhibited this shift. This result can be ascribed to the higher content of the lighter Nb (compared to Ta) in the MLC nanotube lattice. However, one can not preclude the possible contribution of a more efficient charge transfer process from the LaS lattice to the Nb-rich Nb<sub>x</sub>Ta<sub>(1-x)</sub>S<sub>2</sub> lattice (compared with the Ta rich lattice).

Since the concentration of the nanotubes in the product goes down appreciably beyond 60 at% Nb, it was important to try to understand the solid byproducts of the reactions synthesis. Much of the byproduct appeared as platelets, and hence it was surmised that these microcrystallites are either the bulk form of LaS-Nb<sub>x</sub>Ta<sub>(1-x)</sub>S<sub>2</sub> or perhaps pure TaS<sub>2</sub> and NbS<sub>2</sub>, or all. Furthermore, since the Nb content of the nanotubes was rather small up to 60 at% Nb in the precursor, it was anticipated that much of it could be found in the side products of the reaction. EDS/SEM analysis of the platelets confirmed that they contain La, Ta, S and Nb. Furthermore, the Nb concentration was found to increase in the platelets upon increasing the Nb content in the precursors. To that end, Raman analysis of the platelets in the product was undertaken. **Figure 12** shows the Raman analysis of platelets from the reaction with 20 at% Nb (80 at% Ta) content in comparison to that of an MLC tube from this product (green curve). One notices that in general the platelets exhibit

similar spectra to that of the nanotubes. However, an extra peak at 360  $\text{cm}^{-1}$ , which can be assigned to NbS<sub>2</sub>  $A_{1g}$  vibration, is clearly observed in one of the platelets (black curve). The sharp peaks of this particular platelet are indicative of a high crystalline order. In particular, a narrow peak at 140  $\text{cm}^{-1}$  is resolved from the 150  $\text{cm}^{-1}$  peak in the RSII region of this platelet. In the other platelets as well as in the respective nanotube, this peak appears as a left-shoulder to the main 150  $\text{cm}^{-1}$  peak (symmetric  $A_{1g}$  vibration in the RSII zone according to the nomenclature in Ref. 47).

The Raman spectra of platelets belonging to the 40 at% Nb product are quite similar to those of 20 at% Nb content (see **Figure S9**). The 140  $\text{cm}^{-1}$  peak is found to be deconvoluted from the 150  $\text{cm}^{-1}$   $A_{1g}$  peak for the platelet with the sharpest peaks (putatively with the highest crystalline order).

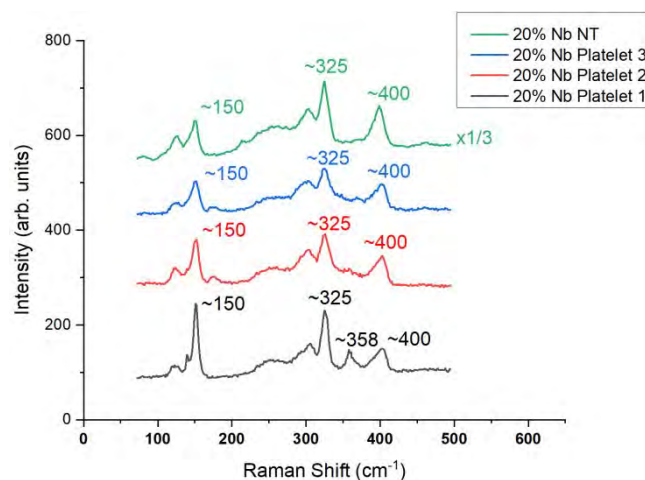


**Figure 12.** Raman spectra of platelets (red, blue and green curves) from the reaction mixture with 20 at% Nb in comparison with a nanotube (black curve) from this reaction mixture.

This analysis indicates that the platelets at this Nb content consist mostly of LaS-Nb<sub>x</sub>Ta<sub>(1-x)</sub>S<sub>2</sub> MLC, but the precise Nb content of the platelets is not known. Most likely the niobium distribution is not the same among the different platelets and is possibly not even uniform within each platelet. **Figure S10** and **Figure S11** display the Raman spectra of the platelets prepared from a precursor containing 60 at% and 80 at% Nb, respectively. In analogy to the nanotubes with high Nb content, the spectra of the high-Nb content platelets, cannot be easily interpreted. However, some of the peaks and in particular the one in 400  $\text{cm}^{-1}$  ( $A_{1g}$  of TaS<sub>2</sub>) is present in all the spectra.

## CONCLUSIONS

Misfit layered compounds (MLC) with the quaternary composition LaS-Nb<sub>x</sub>Ta<sub>(1-x)</sub>S<sub>2</sub> and different Nb content were not studied before. In this work, nanotubes (and platelets) of these quaternary MLC and ascending Nb content were synthesized and analyzed via different electron microscopy methods and Raman spectroscopy. The relative concentration of the nanotubes went down (and that of the platelets increased) with

increasing Nb content. The Nb was found to substitute the Ta atoms, residing on the  $\text{Nb}_x\text{Ta}_{(1-x)}\text{S}_2$  lattice of the MLC. As for other nanotubes from layered (2D) materials, the  $c$ -axis was found to be perpendicular to the growth axis, i.e. in the radial direction of the nanotube. However, in contrast to many cases before, the  $b$ -axis of the MLC lattice did not coincide with the axial (growth) direction of the nanotubes. Notwithstanding their good crystallinity, the analysis verified that the Nb (Ta) distribution in the nanotubes was not uniform along the length of the tubes and also the distance from the surface. The  $1T$  polytype was predominant among the nanotubes prepared from 80 at% Nb. Part of the nanotubes prepared from 80 at% Nb in the precursor exhibited double periodicity (2.35 nm instead of 1.18 nm), which was attributed to the alternating azimuthal orientation of the LaS layers. The nanotubes prepared from precursors containing <60 at% Nb (>40 at% Ta) showed Raman spectra typical for LnS-TaS<sub>2</sub> MLC, while those with larger Nb content exhibited more complex spectra. The Raman spectra of these MLC tubes did not indicate any charge density wave transition.<sup>55</sup> These MLC tubes are expected to reveal interesting quasi-1D physical behavior.

## ASSOCIATED CONTENT

### Supporting Information

Electron diffraction patterns of nanotubes prepared from 20 %at Nb, 40 at% Nb and 80 %at Nb. HR-STEM BF of a nanotube prepared from 80 at% Nb concentration. Results of the EDS quantification performed in various areas of the nanotubes prepared from 80 at% Nb concentration and showing a normal periodicity. Results of the EDS quantification performed in various areas of a nanotube showing a juxtaposition of normal and double periodicity. Results of the EDS quantification performed on two different nanotubes showing a double periodicity. Raman spectra of a few LaS-Nb<sub>x</sub>Ta<sub>(1-x)</sub>S<sub>2</sub> nanotubes prepared from a precursor containing 20, 40, 60 and 80 at% niobium. . Raman spectra of a few MLC LaS-Nb<sub>x</sub>Ta<sub>(1-x)</sub>S<sub>2</sub> platelets prepared from a precursor containing 40, 60 and 80 at% niobium.

This material is available free of charge via the Internet at <http://pubs.acs.org>.

## AUTHOR INFORMATION

### Corresponding Authors

\*E-mail: [luc.lajaunie@uca.es](mailto:luc.lajaunie@uca.es)

\*E-mail: [arenal@unizar.es](mailto:arenal@unizar.es)

\*E-mail: [reshef.tenne@weizmann.ac.il](mailto:reshef.tenne@weizmann.ac.il)

Notes: The authors declare no competing financial interest.

### Author Contributions

<sup>†</sup> D. Stolovas and M. Serra contributed equally to this work

## ACKNOWLEDGMENTS

L.L. acknowledges Dr. Lidia Esther Chinchilla Reyes (University of Cádiz) for the fruitful discussions on microscope alignment and iDPC imaging. We thank Dr. Yishay Feldman for the help with the XRD analysis. Part of the HRSTEM and STEM-EELS studies were conducted at the Laboratorio de Microscopias Avanzadas, Instituto de Nanociencia de Aragon,

Universidad de Zaragoza, Spain. R.A. gratefully acknowledges the support from the Spanish Ministry of Economy and Competitiveness (MINECO) through project grant MAT2016-79776-P (AEI/FEDER, UE). We acknowledge the support of the Irving and Cherna Moskowitz Center for Nano and Bio-Nano Imaging; the Perlman Family Foundation; the Kimmel Center for Nanoscale Science grant No. 43535000350000; the Irving and Azelle Waltcher Foundations in honor of Prof. M. Levy grant No. 720821.

## REFERENCES

- (1) Demichelis, R.; De La Pierre, M.; Mookherjee, M.; Zicovich-Wilson, C. M.; Orlando, R. Serpentine Polymorphism: A Quantitative Insight from First-Principles Calculations. *CrystEngComm* **2016**, *18* (23), 4412–4419.
- (2) Pauling, L. The Structure of the Chlorites. *Proc. Natl. Acad. Sci.* **1930**, *16* (9), 578–582.
- (3) Turkevich, J.; Hillier, J. Electron Microscopy of Colloidal Systems. *Anal. Chem.* **1949**, *21* (4), 475–485.
- (4) Bates, T. F.; Sand, L. B.; Mink, J. F. Tubular Crystals of Chrysotile Asbestos. *Science* **1950**, *111* (2889), 512–513.
- (5) Kroto, H. The Stability of the Fullerenes C<sub>n</sub>, with N= 24, 28, 32, 36, 50, 60 and 70. *Nature* **1987**, *329* (6139), 529.
- (6) Iijima, S. Helical Microtubules of Graphitic Carbon. *nature* **1991**, *354* (6348), 56.
- (7) Tenne, R.; Margulis, L.; Genut, M. e al; Hodes, G. Polyhedral and Cylindrical Structures of Tungsten Disulphide. *Nature* **1992**, *360* (6403), 444–446.
- (8) Višić, B.; Panchakarla, L. S.; Tenne, R. Inorganic Nanotubes and Fullerene-like Nanoparticles at the Crossroads between Solid-State Chemistry and Nanotechnology. *J. Am. Chem. Soc.* **2017**, *139* (37), 12865–12878.
- (9) Makovicky, E.; Hyde, B. Non-Commensurate (Misfit) Layer Structures. In *Inorganic Chemistry; Structure and Bonding*; Springer: Heidelberg, 1981; pp 101–170.
- (10) Wieggers, G. Misfit Layer Compounds: Structures and Physical Properties. *Prog. Solid State Chem.* **1996**, *24* (1), 1–139.
- (11) Panchakarla, L. S.; Radovsky, G.; Houben, L.; Popovitz-Biro, R.; Dunin-Borkowski, R. E.; Tenne, R. Nanotubes from Misfit Layered Compounds: A New Family of Materials with Low Dimensionality. *J. Phys. Chem. Lett.* **2014**, *5* (21), 3724–3736.
- (12) Lajaunie, L.; Ramasubramaniam, A.; Panchakarla, L. S.; Arenal, R. Optoelectronic Properties of Calcium Cobalt Oxide Misfit Nanotubes. *Appl. Phys. Lett.* **2018**, *113* (3), 031102.
- (13) Rouxel, J.; Meerschaut, A.; Wieggers, G. Chalcogenide Misfit Layer Compounds. *J. Alloys Compd.* **1995**, *229* (1), 144–157.
- (14) Bernaerts, D.; Amelinckx, S.; Van Tendeloo, G.; Van Landuyt, J. Microstructure and Formation Mechanism of Cylindrical and Conical Scrolls of the Misfit Layer Compounds PbNb<sub>n</sub>S<sub>2n+1</sub>. *J. Cryst. Growth* **1997**, *172* (3), 433–439.
- (15) van Smaalen, S. Superspace Description of Incommensurate Intergrowth Compounds and the Application to Inorganic Misfit Layer Compounds. In

- Materials Science Forum*; Trans Tech Publ, 1992; Vol. 100, pp 173–222.
- (16) Oosawa, Y.; Gotoh, Y.; Akimoto, J.; Tsunoda, T.; Sohma, M.; Onoda, M. Three Types of Ternary Selenides with Layered Composite Crystal Structures Formed in the Pb-Nb-Se System. *Jpn. J. Appl. Phys.* **1992**, *31* (8A), L1096.
- (17) Rouxel, J.; Moeelo, Y.; Lafond, A.; DiSalvo, F.; Meerschaut, A.; Roesky, R. Role of Vacancies in Misfit Layered Compounds: Case of the Gadolinium Chromium Sulfide Compound. *Inorg. Chem.* **1994**, *33* (15), 3358–3363.
- (18) Gómez-Herrero, A.; Landa-Canovas, A.; Hansen, S.; Otero-Diaz, L. Electron Microscopy Study of Tubular Crystals (BiS)  $1+\delta$  (NbS<sub>2</sub>) N. *Micron* **2000**, *31* (5), 587–595.
- (19) Espinós, J.; González-Elipe, A.; Jumas, J.; Olivier-Fourcade, J.; Morales, J.; Tirado, J.; Lavela, P. 121Sb Mössbauer and X-Ray Photoelectron Spectroscopy Studies of the Electronic Structure of Some Antimony Misfit Layer Compounds. *Chem. Mater.* **1997**, *9* (6), 1393–1398.
- (20) Kars, M.; Fredrickson, D. C.; Gomez-Herrero, A.; Lidin, S.; Rebbah, A.; Otero-Diaz, L. Structural Study by X-Ray Diffraction and Transmission Electron Microscopy of the Misfit Compound (SbS<sub>1-x</sub> XSe<sub>x</sub>) 1.16 (Nb<sub>1-x</sub> 0.36S<sub>2</sub>) 2. *Mater. Res. Bull.* **2010**, *45* (8), 982–988.
- (21) Radovsky, G.; Popovitz-Biro, R.; Stroppa, D. G.; Houben, L.; Tenne, R. Nanotubes from Chalcogenide Misfit Compounds: Sn–S and Nb–Pb–S. *Acc. Chem. Res.* **2014**, *47* (2), 406–416.
- (22) Radovsky, G.; Popovitz-Biro, R.; Lorenz, T.; Joswig, J.-O.; Seifert, G.; Houben, L.; Dunin-Borkowski, R. E.; Tenne, R. Tubular Structures from the LnS–TaS<sub>2</sub> (Ln= La, Ce, Nd, Ho, Er) and LaSe–TaSe<sub>2</sub> Misfit Layered Compounds. *J. Mater. Chem. C* **2016**, *4* (1), 89–98.
- (23) Serra, M.; Stolovas, D.; Houben, L.; Popovitz-Biro, R.; Pinkas, I.; Kampmann, F.; Maultzsch, J.; Joselevich, E.; Tenne, R. Synthesis and Characterization of Nanotubes from Misfit (LnS)<sub>1+y</sub>TaS<sub>2</sub> (Ln= Pr, Sm, Gd, Yb) Compounds. *Chem. Eur. J.* **2018**, *24* (44), 11354–11363.
- (24) Meerschaut, A.; Rabu, P.; Rouxel, J.; Monceau, P.; Smontara, A. Structural Reinvestigation of (LaS)<sub>1.14</sub>NbS<sub>2</sub> and Resistivity Measurements. *Mater. Res. Bull.* **1990**, *25* (7), 855–861.
- (25) Wieggers, G.; Meetsma, A.; Van Smaalen, S.; Haange, R.; Wulff, J.; Zeinstra, T.; De Boer, J.; Kuypers, S.; Van Tendeloo, G.; Van Landuyt, J.; et al. Misfit Layer Compounds (MS)<sub>N</sub>TS<sub>2</sub> (M= Sn, Pb, Bi, Rare Earth Elements; T= Nb, Ta; N= 1.08–1.19), a New Class of Layer Compounds. *Solid State Commun.* **1989**, *70* (4), 409–413.
- (26) De Boer, J.; Meetsma, A.; Zeinstra, T. J.; Haange, R.; Wieggers, G. Structures of the Misfit Layer Compounds (LaS)<sub>1.13</sub> TaS<sub>2</sub>, 'LaTaS3' and (CeS)<sub>1.5</sub>TaS<sub>2</sub>, 'CeTaS3'. *Acta Crystallogr. Sect. C* **1991**, *47* (5), 924–930.
- (27) Madhukar, A. Structural Classification of Layered Dichalcogenides of Group IV B, VB and VI B Transition Metals. *Solid State Commun.* **1975**, *16* (4), 383–388.
- (28) Herber, R. H.; Katada, M. Lattice Dynamics and Hyperfine Interactions of the Intercalation Compounds: NbS<sub>2</sub>·Sn and NbS<sub>2</sub>·Sn<sub>13</sub>. *J. Solid State Chem.* **1979**, *27* (2), 137–144.
- (29) Lieber, C. M.; Wu, X. L. Scanning Tunneling Microscopy Studies of Low-Dimensional Materials: Probing the Effects of Chemical Substitution at the Atomic Level. *Acc. Chem. Res.* **1991**, *24* (6), 170–177.
- (30) Lucking, M. C.; Beach, K.; Terrones, H. Large Second Harmonic Generation in Alloyed TMDs and Boron Nitride Nanostructures. *Sci. Rep.* **2018**, *8* (1), 10118.
- (31) Peña, F. de la; Burdet, P.; Ostasevicius, T.; Sarahan, M.; Nord, M.; Taillon, V. T. F. J.; Eljarrat, A.; Mazzucco, S.; Donval, G.; Zagonel, L. F.; et al. *HyperSpy: Multidimensional Data Analysis Toolbox*; 2015.
- (32) Ewels, P.; Sikora, T.; Serin, V.; Ewels, C. P.; Lajaunie, L. A Complete Overhaul of the Electron Energy-Loss Spectroscopy and X-Ray Absorption Spectroscopy Database: Eelsdb. *Eu. Microsc. Microanal.* **2016**, *22* (3), 717–724.
- (33) Lazić, I.; Bosch, E. G.; Lazar, S. Phase Contrast STEM for Thin Samples: Integrated Differential Phase Contrast. *Ultramicroscopy* **2016**, *160*, 265–280.
- (34) Wieggers, G.; Meetsma, A.; Haange, R.; De Boer, J. Crystal Growth, Structure and Some Properties of PbNbS<sub>3</sub>, SnSnNbS<sub>3</sub>, LaNbS<sub>3</sub> and Related Misfit Layer Compounds. *Solid State Ion.* **1989**, *32*, 183–191.
- (35) Shannon, R. D. Revised Effective Ionic Radii and Systematic Studies of Interatomic Distances in Halides and Chalcogenides. *Acta Crystallogr. A* **1976**, *32* (5), 751–767.
- (36) Wilson, J.; Yoffe, A. The Transition Metal Dichalcogenides Discussion and Interpretation of the Observed Optical, Electrical and Structural Properties. *Adv. Phys.* **1969**, *18* (73), 193–335.
- (37) Radovsky, G.; Popovitz-Biro, R.; Tenne, R. Nanotubes from the Misfit Layered Compounds MS-TaS<sub>2</sub>, Where M= Pb, Sn, Sb and Bi: Synthesis and Study of Their Structure. *Chem. Mater.* **2014**, *26* (12), 3757–3770.
- (38) Houben, L.; Enyashin, A.; Feldman, Y.; Rosentsveig, R.; Stroppa, D.; Bar-Sadan, M. Diffraction from Disordered Stacking Sequences in MoS<sub>2</sub> and WS<sub>2</sub> Fullerenes and Nanotubes. *J. Phys. Chem. C* **2012**, *116* (45), 24350–24357.
- (39) Kraxner, J.; Schäfer, M.; Röschel, O.; Kothleitner, G.; Haberkühner, G.; Paller, M.; Grogger, W. Quantitative EDXS: Influence of Geometry on a Four Detector System. *Ultramicroscopy* **2017**, *172*, 30–39.
- (40) Sadoway, D. R.; Flengas, S. Vapour Pressures of Solid and Liquid NbCl<sub>5</sub> and TaCl<sub>5</sub>. *Can. J. Chem.* **1976**, *54* (11), 1692–1699.
- (41) Gauquelin, N.; Van den Bos, K.; Béché, A.; Krause, F.; Lobato, I.; Lazar, S.; Rosenauer, A.; Van Aert, S.; Verbeeck, J. Determining Oxygen Relaxations at an Interface: A Comparative Study between Transmission Electron Microscopy Techniques. *Ultramicroscopy* **2017**, *181*, 178–190.
- (42) Lajaunie, L.; Boucher, F.; Dessapt, R.; Moreau, P. Quantitative Use of Electron Energy-Loss Spectroscopy Mo-M<sub>2,3</sub> Edges for the Study of Molybdenum Oxides. *Ultramicroscopy* **2015**, *149*, 1–8.

- 1  
2  
3  
4  
5  
6  
7  
8  
9  
10  
11  
12  
13  
14  
15  
16  
17  
18  
19  
20  
21  
22  
23  
24  
25  
26  
27  
28  
29  
30  
31  
32  
33  
34  
35  
36  
37  
38  
39  
40  
41  
42  
43  
44  
45  
46  
47  
48  
49  
50  
51  
52  
53  
54  
55  
56  
57  
58  
59  
60
- (43) Panchakarla, L. S.; Lajaunie, L.; Tenne, R.; Arenal, R. Atomic Structural Studies on Thin Single-Crystalline Misfit-Layered Nanotubes of TbS-CrS<sub>2</sub>. *J. Phys. Chem. C* **2016**, *120* (29), 15600–15607.
- (44) Panchakarla, L. S.; Lajaunie, L.; Ramasubramaniam, A.; Arenal, R.; Tenne, R. Nanotubes from Oxide-Based Misfit Family: The Case of Calcium Cobalt Oxide. *ACS Nano* **2016**, *10* (6), 6248–6256.
- (45) Panchakarla, L. S.; Lajaunie, L.; Ramasubramaniam, A.; Arenal, R.; Tenne, R. Strontium Cobalt Oxide Misfit Nanotubes. *Chem. Mater.* **2016**, *28* (24), 9150–9157.
- (46) Lajaunie, L.; Radovsky, G.; Tenne, R.; Arenal, R. Quaternary Chalcogenide-Based Misfit Nanotubes LnS(Se)-TaS(Se)<sub>2</sub> (Ln = La, Ce, Nd, and Ho): Synthesis and Atomic Structural Studies. *Inorg. Chem.* **2018**, *57* (2), 747–753.
- (47) Kisoda, K.; Hangyo, M.; Nakashima, S.; Suzuki, K.; Enoki, T.; Ohno, Y. Raman Scattering from Misfit Layer Compounds (RS)<sub>x</sub>TaS<sub>2</sub> (R Identical to La, Ce, Sm or Gd; S Identical to Sulphur; x Approximately=1.2). *J. Phys. Condens. Matter* **1995**, *7* (27), 5383.
- (48) Staiger, M.; Bačić, V.; Gillen, R.; Radovsky, G.; Gartsman, K.; Tenne, R.; Heine, T.; Maultzsch, J.; Thomsen, C. Raman Spectroscopy of Intercalated and Misfit Layer Nanotubes. *Phys. Rev. B* **2016**, *94* (3), 035430.
- (49) Nakashima, S.; Tokuda, Y.; Mitsuishi, A.; Aoki, R.; Hamaue, Y. Raman Scattering from 2H-NbS<sub>2</sub> and Intercalated NbS<sub>2</sub>. *Solid State Commun.* **1982**, *42* (8), 601–604.
- (50) McMullan, W.; Irwin, J. Raman Scattering from 2H and 3R-NbS<sub>2</sub>. *Solid State Commun.* **1983**, *45* (7), 557–560.
- (51) Carmalt, C. J.; Manning, T. D.; Parkin, I. P.; Peters, E. S.; Hector, A. L. Formation of a New (1T) Trigonal NbS<sub>2</sub> Polytype via Atmospheric Pressure Chemical Vapour Deposition. *J. Mater. Chem.* **2004**, *14* (3), 290–291.
- (52) Sugai, S.; Murase, K.; Uchida, S.; Tanaka, S. Studies of Lattice Dynamics in 2H-TaS<sub>2</sub> by Raman Scattering. *Solid State Commun.* **1981**, *40* (4), 399–401.
- (53) Smith Jr, J.; Tsang, J.; Shafer, M. Raman Spectra of Several Layer Compounds with Charge Density Waves. *Solid State Commun.* **1976**, *19* (4), 283–286.
- (54) Hangyo, M.; Nakashima, S.-I.; Mitsuishi, A. Raman Spectroscopic Studies of MX<sub>2</sub>-Type Layered Compounds. *Ferroelectrics* **1983**, *52* (1), 151–159.

1 SYNOPSIS TOC  
2  
3  
4

